



Cite this: *RSC Adv.*, 2021, 11, 34117

# Production of nitrogen-doped carbon quantum dots with controllable emission wavelength, excellent sensing of Fe<sup>3+</sup> in aqueous solution, and potential application for stealth quick response coding in the visible regime†

Yu-Hsun Su, Hsuan-Hao Huang, Chao-Chi Tseng, Hsin-Jung Tsai and Wen-Kuang Hsu \*

Received 2nd July 2021  
Accepted 27th September 2021

DOI: 10.1039/d1ra05106g

rsc.li/rsc-advances

Nitrogen-doped carbon quantum dots (N-CQDs) exhibit a high quantum yield with controllable emission wavelength and intensity in the blue-green regime. N-CQDs were tested and determined to be thermally and optically stable during 150 °C heat treatment and prolonged UV irradiation. Potential applications of N-CQDs were demonstrated, including excellent Fe<sup>3+</sup> sensing in aqueous solution, fluorescent polymer fibres, and stealth quick response coding at visible wavelengths.

## 1 Introduction

Quantum dots (QDs) show great potential for imaging applications and are mostly made of semiconductor materials.<sup>1</sup> However, the production process for QDs is lengthy, and in particular, the toxicity of QDs remains to be addressed.<sup>2,3</sup> Carbon materials including graphite, carbon fibres, carbon nanotubes, graphene, carbon black, activated carbon, and fullerenes are sp<sup>2</sup>-bonded structures and are now widely used.<sup>4–12</sup> There has been great interest in carbon quantum dots (CQDs) because they represent a new class of fluorescent nanomaterials mainly due to their water solubility, eco-friendliness, ability to be processed with ease, and low synthetic cost.<sup>13–15</sup> Reports indicate that CQDs can be used in bio-imaging,<sup>16,17</sup> anti-counterfeiting,<sup>18</sup> photocatalysis,<sup>19,20</sup> chemical sensing,<sup>21–23</sup> drug delivery,<sup>24</sup> light-emitting diodes,<sup>17,25</sup> and energy technology.<sup>26</sup> For example, perovskite solar cells can be inexpensively produced and show high power conversion efficiency.<sup>3,27–30</sup> However, devices suffer greatly from dangling edge-induced carrier recombination, which thus lowers performance. Uncoordinated ions may be passivated by oxygenated groups of CQDs, which in turn reduce non-radiative processes. CQD production currently relies on top-down and bottom-up techniques. The former is achieved through break-down of large carbon masses into nano-sized clusters, using techniques such as arc discharge,<sup>31</sup> laser ablation,<sup>32</sup> and high

energy ball milling.<sup>33</sup> The top-down method is also time-consuming, with a quantum yield (QY) lower than 10%. The bottom-up approach uses organic molecules as precursors and produces CQDs through different routes, including solvothermal reactions (ST),<sup>34–36</sup> microwave-assisted pyrolysis,<sup>37</sup> heterogeneous reactions (HR),<sup>38</sup> and combustion (Table 1).<sup>39</sup>

Chemical doping is a technique capable of modifying the band diagram of solids and has been applied to carbon materials.<sup>40,41</sup> Studies have revealed that nitrogen-doping increases the photoluminescence (PL) of CQDs, and the underlying mechanism involves the creation of optical states around the band edges.<sup>42,43</sup> Attributed to lone-pair electrons, nitrogen-doped CQDs (N-CQDs) behave as conjugated bases and are highly sensitive to cations in aqueous solution.<sup>44–47</sup> N-CQDs can be made by ST using organic precursors, such as citric acid (CA), ammonium citrate, L-cysteine, urea (UA), ethylenediamine, and hexamethylenetetramine.<sup>48–52</sup> Reports indicate that CQDs produced in organic solvents emit mostly green-red light, while the emission wavelength ( $E_{\lambda}$ ) of CQDs produced in water is essentially limited to blue.<sup>53–55</sup>

In this work, blue-green emission (420–500 nm) from CQDs is achieved through adjustment of the N-doping content as follows. First, N-CQDs are produced using mixed precursors (CA + UA); the former provides the carbon source, and the latter provides N-doping. Note that because UA is inexpensive, we therefore selected it as a precursor. Second, the doping content is controlled by tuning of the UA/CA ratio. We found that  $E_{\lambda}$  varied with UA/CA, and the QY reached a value as high as 36% in 395 nm excitation energy ( $E_{\text{ex}}$ ). Incorporation of N-CQDs into polyvinyl alcohol (PVA) and polystyrene (PS) produces luminescent polymer films and fibres; the latter is made by an electrospinning technique that does not involve high

Department of Materials Science and Engineering, High Entropy Materials Centre, National Tsing-Hua University, Hsinchu 300044, Taiwan. E-mail: wkhsu@mx.nthu.edu.tw

† Electronic supplementary information (ESI) available: Carbon quantum dots, electrospinning, ion sensing, fluorescent labelling. See DOI: 10.1039/d1ra05106g



Table 1 Synthetic methods and related parameters for CQDs

	Top-down routes	Bottom-up routes
Precursors	• Large carbon masses (such as CNT-s, activated carbon, graphite, and carbon fiber)	• Small organic molecules
Methods	• Arc discharge • Laser ablation • Electrochemical synthesis • High-energy ball milling	• Solvothermal/hydrothermal • Microwave • Chemical vapor deposition • Heterogeneous reaction
Characteristics	• Low quantum yields	• Heteroatom doping • Tuneable emission wavelength

Table 2 Synthetic parameters for ST (top) and HR (lower)

Sample	CA (g)	UA (g)	Molar ratio (UA/CA)	Solvent	Conditions	Product mass (g)
ST1	0.4	0.125	1	H <sub>2</sub> O	150 °C, 2 h	0.094
ST3		0.375	3			0.270
ST7		0.875	7			0.314
ST15		1.875	15			0.339
ST30		3.75	30			0.303
ST60		7.5	60			0.228
ST15et		1.875	15	Ethanol		0.212

Sample	CA (g)	UA (g)	Molar ratio (UA/CA)	Temperature (°C)	Time (h)	Product mass (g)
HR2	0.4	0.25	2	160	4	0.138
HR5		0.625	5			0.204
HR10		1.25	10			0.281
HR15		1.875	15			0.266
HR15 <sub>II</sub>		1.875	15	150	4	0.245
HR15 <sub>III</sub>					2	0.232
HR15 <sub>IV</sub>					0.5	0.073
HR15 <sub>V</sub>				135	4	0.187

temperature or coagulation processes. Applications of N-CQDs are also demonstrated, including sensing of Fe<sup>3+</sup> in aqueous solution and stealth QR coding and labelling in the visible regime.

## 2 Experimental section

### 2.1 Materials

Anhydrous CA, UA, and metal salts NaCl, KCl, MgCl<sub>2</sub>, CaCl<sub>2</sub>, FeCl<sub>2</sub>, FeCl<sub>3</sub>, CuSO<sub>4</sub>, Zn(NO<sub>3</sub>)<sub>2</sub>, Pb(NO<sub>3</sub>)<sub>2</sub>, CrCl<sub>3</sub>, Co(NO<sub>3</sub>)<sub>2</sub>, and Ni(NO<sub>3</sub>)<sub>2</sub> were purchased from Showa Chemical Industry Co., Ltd. PVA (*M<sub>w</sub>* = 121 000) and PS (*M<sub>w</sub>* = 192 000) were purchased from the First Chemical Works (Taiwan) and Sigma-Aldrich. E-132 epoxy resin and H-TK curing agent were obtained from Fong Yong Chemical Co., Ltd. Light fabric transfer papers were purchased from Upsilon Enterprise Co., Ltd.

### 2.2 Synthetic procedures for ST

CA and UA, mixed respectively in a molar ratio of 1, 3, 7, 15, 30, and 60 (hereafter defined as ST1, ST3, ST7, ST15, ST30, and ST60), were dissolved in deionized water (10 ml) (top, Table 2). The solution was loaded into a Teflon-lined stainless steel autoclave and heated at 150 °C for 2 h. After cooling to room

temperature, the treated solution was mixed with ethanol (200 ml), followed by sonication for 5 min, and centrifugation at 6000 rpm for 15 min. The precipitates were dried at 70 °C, and were then re-dispersed in water (Fig. 1a). Removal of the aqueous solution resulted in a production yield of 4–6 wt%.

### 2.3 Synthetic procedures for HR

CA and UA, mixed in molar ratios of 2, 5, 10, and 15 (hereafter defined as HR2, HR5, HR10, and HR15, lower, Table 2), were ground in an agate mortar. The mixture was transferred to

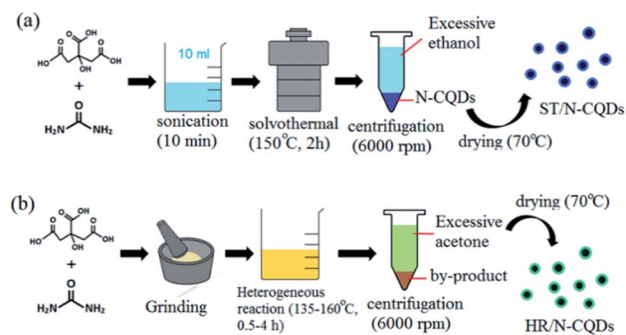


Fig. 1 Synthetic procedures for (a) ST and (b) HR.



a glass bottle and was aerielly heated at 160 °C for 4 h. After cooling to room temperature, the resultant dark powder was dispersed in deionized water and acetone (50 ml), followed by sonication for 10 min and centrifugation at 6000 rpm for 15 min. The upper-layer suspension was dried at 70 °C and was then re-dispersed in acetone and/or water (Fig. 1b). Removal of solution resulted in a production yield of 4–6 wt%, with the product resembling ST-made CQDs.

#### 2.4 Fabrication of HR15/PVA composite films

HR15 (12.5 mg) and PVA (2.5 g) were mixed in deionized water (12.5 ml), followed by magnetic stirring at 90 °C for 3 h to attain a homogeneous solution. The solution was transferred onto a glass slide and was dried under a fume hood for a day to obtain a HR15/PVA composite film.

#### 2.5 Fabrication of HR15/PVA and HR15/PS composite fibres

HR15/PVA composite fibres are prepared as follows. HR15 (4 wt%), PVA (5 wt%), and dimethyl sulfoxide (DMSO, 15 wt%) were dissolved in water and were magnetically stirred at 90 °C for 3 h to attain a homogeneous solution. The solution was subjected to electrospinning at 24 kV with a working distance of 10 cm and feeding rate of 1 ml h<sup>-1</sup> (top, Table 3). HR15/PS composite fibres were also fabricated by an electrospinning technique. PS was first melted in mixed solvents (toluene/acetone, 8 : 2), followed by HR15 addition. Due to viscosity arising from PS, the electrospinning was carried out at 20 kV with working distance and feeding rate of 10 cm and 3.5 ml h<sup>-1</sup>, respectively (lower, Table 3).

#### 2.6 Thermal stability

The thermal stability of the HR15/PVA composite films, HR15, and ST3 was tested as follows. First, samples were heated at 75, 100, 125, 150, 175, 200, 225, and 250 °C for 1 h. Second, PL emission intensity ( $E_i$ ), and  $E_\lambda$  were compared before and after heat treatments. Note that comparisons were made on the basis of similar concentrations and conditions, *i.e.*, ST3/water (0.5 mg ml<sup>-1</sup>), HR15/acetone (0.1 mg ml<sup>-1</sup>), and HR15/water (0.5 mg ml<sup>-1</sup>). Third, the solution was illuminated by 365 nm UV lamp at the distance of 5 cm, and PL spectra were recorded for 2, 4, 6, 8, 10, 12, and 24 h.

#### 2.7 Sensing of Fe<sup>3+</sup> in aqueous solution

Different concentrations of Fe<sup>3+</sup> (0–500 μM) were added to 0.4 μg ml<sup>-1</sup> HR15 aqueous solution, followed by PL recording at  $E_{ex}$  = 395 nm (=3.138 eV). The selectivity of Fe<sup>3+</sup> was investigated by adding 12 types of metal ions with concentrations of 1 mM (Na<sup>+</sup>, K<sup>+</sup>, Mg<sup>2+</sup>, Ca<sup>2+</sup>, Fe<sup>2+</sup>, Fe<sup>3+</sup>, Co<sup>2+</sup>, Ni<sup>2+</sup>, Cu<sup>2+</sup>, Zn<sup>2+</sup>, Cr<sup>3+</sup>, and Pb<sup>2+</sup>) to 4 μg ml<sup>-1</sup> HR15 aqueous solution.

#### 2.8 Instrumental analyses

The ultraviolet-visible (UV-Vis) absorption spectra and PL spectra were recorded by a Hitachi U-2010 spectrophotometer and PerkinElmer LS-55 luminescence spectrometer. Transmission electron microscopy (TEM, JEOL, JEM-ARM200FTH) and electron diffraction (Gatan Microscopy Suite software) were employed to analyse structures of ST- and HR-produced CQDs, in conjunction with X-ray diffraction (XRD, Bruker D2 Phaser under Cu-Kα radiation,  $\lambda$  = 1.5406 Å, 2θ mode), Fourier transform infrared spectroscopy (FTIR, Horiba FT-730 spectrometer), Raman spectroscopy (Horiba LabRAM HR800 spectrometer with He-Ne laser at 632.8 nm wavelength), optical microscopy (Microtech MX53 microscope), and scanning electron microscopy (SEM). Energy-dispersive X-ray spectroscopy (EDX, Hitachi SU-8010 electron microscope) and X-ray photoelectron emission spectroscopy (XPS, ULVAC-PHI PHI 5000 Versaprobe II) were used for elemental analyses.

#### 2.9 QY measurements

QY was calculated according to the equation  $QY = QY' \times (m/m') \times (n_2/n_2')$ , where  $m$  denotes the profile slope of  $E_i$  against absorbance and is determined using quinine sulfate as a reference.<sup>56</sup> The  $n$  denotes the refraction index, and is 1.33 for water and 1.36 for acetone.

### 3 Results and discussion

#### 3.1 Characterization of CQD structures

TEM images indicate that samples produced by HR or ST consist of spherical nanoparticles embedded in an amorphous carbon matrix (Fig. 2a). Particles consist of layered structures, where the (002) and (110) diffraction vectors originate from inter-layer spacing (3.4 Å) and zigzag lines of graphite sheets

**Table 3** Electrospinning parameters for HR15/PVA (top) and HR15/PS fibres (lower)

$C_{HR15/PVA}$	Solvent ratio (DMSO/water)	$C_{solution}$	Work distance	Voltage	Flow rate
4 wt%	0 : 10	5 wt%	10 cm	24 kV	1 ml h <sup>-1</sup>
	0 : 10	8 wt%			
	1.5 : 10	8 wt%			
$C_{HR15/PS}$	Solvent ratio (toluene/acetone)	$C_{solution}$	Work distance	Voltage	Flow rate
2 wt%	2 : 8	5 wt%	10 cm	20 kV	3.5 ml h <sup>-1</sup>
4 wt%					
8 wt%					



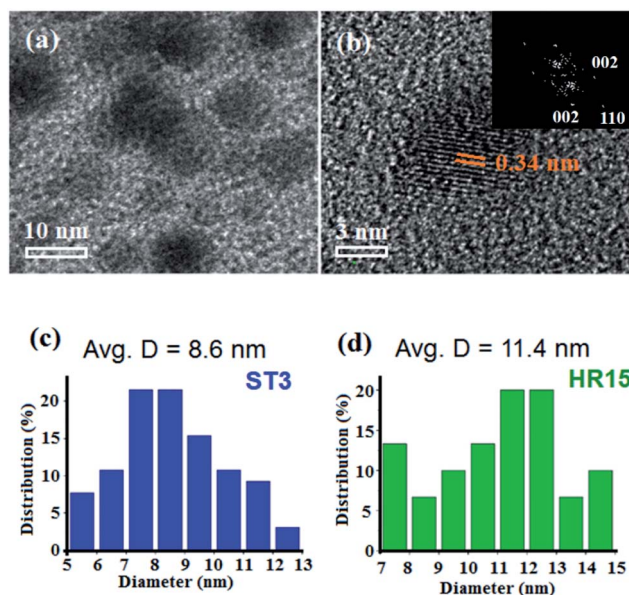


Fig. 2 (a) HRTEM image of HR-CQDs. (b) Magnified image of a selected HR-CQD and electron diffraction pattern (top right inset). Diameter distribution of (c) ST3 and (d) HR15.

(2.1 Å) (Fig. 2b).<sup>57</sup> TEM further reveals that the average diameter is  $8.6 \pm 3.5$  nm for ST3- and  $11.4 \pm 3.2$  nm for HR15-made CQDs (Fig. 2c and d). TEM images of ST-made CQDs are shown in Fig. S1 (ESI†).

The (002) reflection was also observed in XRD, along with profiles arising from  $sp^2$ - $sp^3$  hybrids (4.9 Å) and graphite oxide (6.4 Å) (Fig. 3a).<sup>58–60</sup> Note that the (002) bandwidth of ST-made CQDs is broad, indicative of an amorphous governed structure (Fig. 3a). HR-created N-doping is evident by (i) Raman, (ii) FTIR, and (iii) EDX as follows. First, doping produces lattice defects, thus giving  $I_D/I_G \propto UA/CA$ , where  $I_D$  and  $I_G$  represent the intensity of Raman D ( $1340\text{ cm}^{-1}$ ) and G ( $1570\text{ cm}^{-1}$ ) bands; the former is due to phonon scattering by defects/zone boundaries, and the latter is due to the vibration of  $sp^2$ -bonded carbons (Fig. 3b).<sup>61</sup> Second, the stretching mode of N–H ( $3348\text{ cm}^{-1}$ ) and O–H ( $3200\text{ cm}^{-1}$ ) was observed *via* FTIR spectroscopy, along with stretching ( $2800\text{ cm}^{-1}$ ) and bending ( $760\text{ cm}^{-1}$ ) of C–H and vibrations of C=O ( $1713\text{ cm}^{-1}$ ), C=C ( $1600\text{ cm}^{-1}$ ), C–N ( $1368\text{ cm}^{-1}$ ), and C–O ( $1060\text{ cm}^{-1}$ )

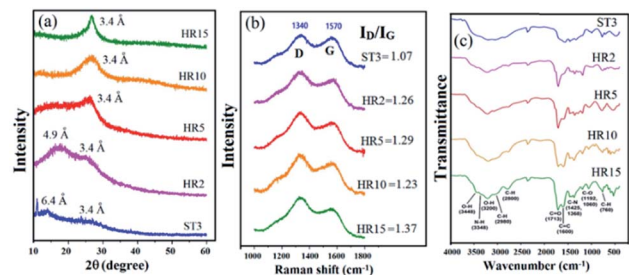


Fig. 3 (a) XRD, (b) Raman, and (c) FTIR spectra of CQDs made by ST and HR.

Table 4 Elemental analyses of ST- and HR-made CQDs

Samples	C (at%)	O (at%)	N (at%)	C/O
ST3	70.9	29.1	0	2.44
HR2	59.2	31.3	9.5	1.89
HR5	56.0	32.6	11.4	1.72
HR10	46.7	37.6	15.7	1.24
HR15	50.4	29.4	20.2	1.71

(Fig. 3c).<sup>62,63</sup> Third, EDX confirmed the presence of C, O, and N signals with a C/O ratio greater than UA (1.00) and CA (0.86), which is indicative of dehydration during N-CQD formation (Table 4). Four, the doping content  $\propto UA/CA$  again verifies the presence of UA-created N-doping (Table 4). However, doping is absent in ST3, accounting for lower  $I_D/I_G$  and greater C/O ratios (Fig. 3c and Table 4). Fig. S2† shows the XPS results for ST3 and HR15; the latter displays a greater content of N-dopants according to peak area integration (ESI†).

### 3.2 PL of CQDs

Fig. 4a and b displays the PL spectra and optical images of ST-CQDs-dispersed water (right inset). Clearly, all samples emit blue-green light with a similar full width at half maximum (FWHM = 65 nm) and peak centre ( $E_{\lambda C} = 440\text{ nm}$ ), indicating that  $E_{ex}$  and the UA/CA ratio have no effect on  $E_{\lambda}$  tuning.  $E_1$ , however, varies with UA/CA and follows the sequence ST3 > ST7 > ST15 > ST30 > ST1. Because emission involves radiative processes around band edges, it is important to understand how optical transitions proceed in CQDs. Fig. 4c displays the UV-Vis spectra of ST-made CQDs, where the absorption at 200–211 nm is attributed to the  $\pi$ - $\pi^*$  transition of C=C/C–C bonds in the  $sp^2$ -hybridized domains and barely contributes to PL.<sup>13</sup> The peak at 335 nm originates from the  $n_O$ - $\pi^*$  transition of C=O/C–OH bonds in amorphous regions, where  $n_O$  denotes the radiative relaxation of excited lone pairs in oxygen and significantly contributes to blue emission.<sup>64</sup> By using quinine sulfate/0.1 M  $H_2SO_4$  solution as a reference, the QY of ST3 was determined to be 37.5% and 23.3% for  $E_{ex} = 365$  and 395 nm, respectively (Fig. S3, ESI†).

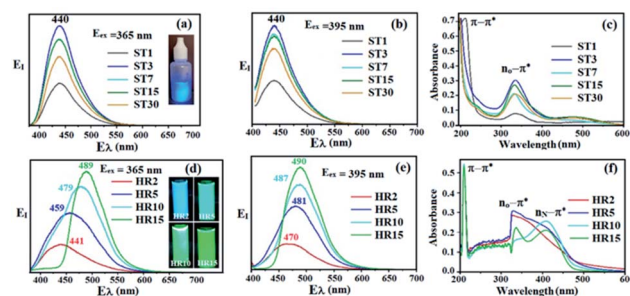


Fig. 4 (a–c) 365 and 395 nm excited  $E_1$ – $E_2$  and UV-Vis spectra of ST-made CQDs. (d–f) 365 and 395 nm excited  $E_1$ – $E_2$  and UV-Vis spectra of HR-made CQDs.



**Table 5**  $E_{\lambda C}$ , FWHM and QY of HR15/acetone and HR15/water measured at  $E_{ex} = 395$  nm

Sample	$E_{ex} = 365$ nm		
	$E_{\lambda C}$	FWHM	QY
HR15/acetone	441	92	10.2%
HR15/water	459	105	23.8%

HR-made N-CQDs show  $E_1 \propto \text{UA/CA}$ , indicative of additional emission from N-doped structures (Fig. 4d and e).<sup>65</sup> The  $E_{\lambda C}$  also varies with UA/CA and  $E_{ex}$ , *i.e.*,  $E_{\lambda C} = 441$  (HR2), 459 (HR5), 479 (HR10), and 489 nm (HR15) for  $E_{ex} = 365$  nm (right insets, Fig. 4d). At  $E_{ex} = 395$  nm, the  $E_{\lambda C}$  redshifts to 470 (HR2), 481 (HR5), 487 (HR10), and 490 nm (HR15), verifying the movement of absorption edges to long wavelengths (Fig. 4d and e). The UV-Vis spectra confirmed that doping induced an  $n_N-\pi^*$  transition of C–N bonds in amorphous regions (408 nm), where  $n_N$  denotes radiative relaxation of excited lone pairs in nitrogen, accounting for the emission of greenish light and red-shifted  $E_{\lambda C}$  (Fig. 4f).<sup>65</sup> The QY of HR-acetone exceeds that of HR-water, and the UA/CA  $\propto$  QY relation again supports improved PL (Tables 5 and 6, and Fig. S3, ESI†).

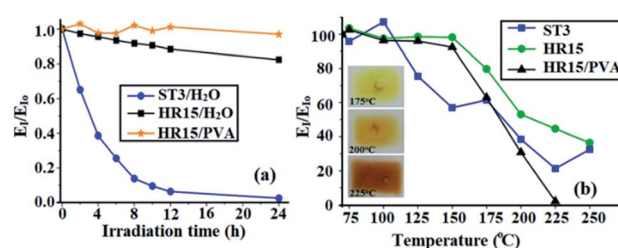
Due to radiolysis and oxidation, conventional QDs barely survive under prolonged UV irradiation and heat treatments.<sup>25</sup> Here, ST3 and HR15 were selected for 365 nm irradiation and thermal stability tests because both show the highest QY in their own groups. Fig. 5a plots  $E_1/E_{10}$  against irradiation time, and measurements were performed with 5 W of lighting power at a distance of 10 cm from the samples. Clearly, ST3 rapidly degrades, and  $E_1/E_{10}$  decreases to 40% in 4 h, 12% in 8 h, 8% in 12 h, and 3% in 24 h. In contrast, HR15–H<sub>2</sub>O and HR15–PVA display a high  $E_1/E_{10}$  after 24 h, with measurements indicating 82.4% and 97% (Fig. S4, ESI†). In the thermal stability tests, the  $E_1/E_{10}$  of ST3 begins to decrease at approximately 100 °C and decreases to 21.3% at 225 °C (Fig. 5b). HR15, in contrast, is thermally stable prior to 150 °C, where  $E_1/E_{10}$  is decreased by less than 2%. The  $E_1/E_{10}$  then decreases to 44.6% and 2% at 225 °C for HR15 and HR15–PVA, respectively; the latter is attributed to the thermal decomposition of polymer that induces optical shielding, thus compromising  $E_1$  (left insets, Fig. 5b and S5, ESI†).

### 3.3 Applications of CQDs

PL pigments are now widely used and are mostly made from organic compounds such as stilbene-, benzimidazole-,

**Table 6**  $E_{\lambda C}$ , FWHM, and QY of HR2, HR5, HR10, and HR15 measured at  $E_{ex} = 365$  and 395 nm

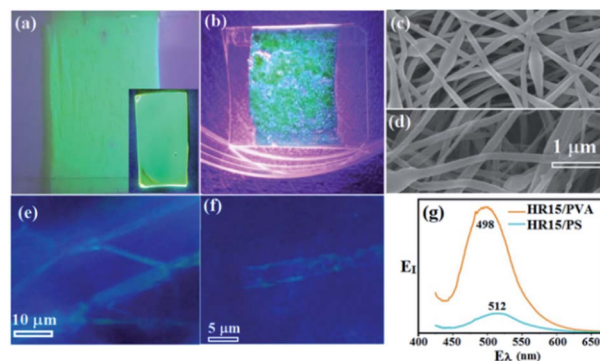
Sample	$E_{ex} = 365$ nm			$E_{ex} = 395$ nm		
	$E_{\lambda C}$	FWHM	QY	$E_{\lambda C}$	FWHM	QY
HR2	441	92	10.2%	470	85	10.3%
HR5	459	105	23.8%	481	83	25.3%
HR10	479	96	34.2%	487	74	33.0%
HR15	489	71	30.5%	490	71	36.0%

**Fig. 5** (a)  $E_1/E_{10}$  vs. UV-irradiation time and (b)  $E_1/E_{10}$  vs. temperature of CQDs.

coumarin-, and II–VI, III–V, and IV–VI group-based. However, the cited compounds lack thermal stability, and in particular, the issue concerning carcinogenicity remains to be addressed.<sup>66,67</sup> The data above clearly show that HR-CQDs exhibit superior thermal and optical properties and were therefore selected to demonstrate their potential applications, including PL polymer fibres, sensing of  $\text{Fe}^{3+}$  in aqueous solution, and stealth QR coding and labelling in the visible regime.

**3.3.1 CQDs-polymer fibres and films.** Fig. 6 displays optical images of 395 nm-excited (a) HR15/PVA and (b) CQDs/PS fibres, along with SEM images taken at 500 $\times$  magnification (Fig. 6c and d). There is a similar aspect ratio for both types of fibres, which is attributed to their hydrophilic nature and satisfactory wetting, and the CQDs were well dispersed in PVA.<sup>68,69</sup> First, the PL was uniform relative to HR15/PS. Second, uniform PL was also present in the HR15/PVA films (inset, Fig. 6a). Third, magnified images confirm that PL was emitted from regions contiguous to surfaces. Fourth, HR15/PVA exhibits a greater fibre density compared with HR15/PS (Fig. 6e and f). Fifth, the  $E_1-E_{\lambda}$  plot supports the descriptions above, which indicates that CQDs are well dispersed in PVA, and thus provide a greater  $E_1$ ; the measured  $E_{\lambda C}$  was 498 nm for HR15/PVA and 512 nm for HR15/PS (Fig. 6g).

**3.3.2 Sensing of  $\text{Fe}^{3+}$  in aqueous solution by CQDs.** Sensing and detection limits of  $\text{Fe}^{3+}$  were determined by the  $3\sigma$  method in 0.4 mg ml<sup>−1</sup> HR15 aqueous solution.<sup>70</sup> First, a quenching

**Fig. 6** Optical images of 395 nm-excited electrospinning-made (a) HR15/PVA and (b) HR15/PS fibre mats. SEM images of (c) HR15/PVA and (d) HR15/PS fibres. Enlarged optical images of 395 nm-excited (e) HR15/PVA and (f) HR15/PS fibres. (g)  $E_1-E_{\lambda}$  plot of HR15/PVA and HR15/PS fibres.

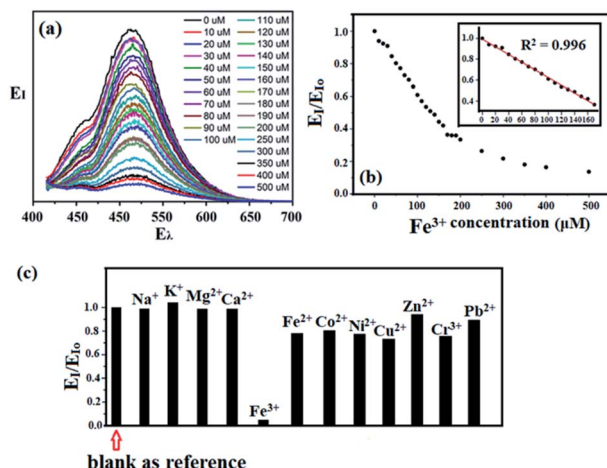


Fig. 7 (a)  $E_1$ - $E_\lambda$  plot against  $\text{Fe}^{3+}$  concentration, (b)  $E_1/E_{10}$  vs.  $\text{Fe}^{3+}$  concentration and highlighted profile at 0–170  $\mu\text{M}$  (inset), and (c) comparison of  $\text{Fe}^{3+}$ -induced  $E_1/E_{10}$  reduction with others.

effect appeared, which was evident by the  $E_1$  decrease with increasing  $\text{Fe}^{3+}$  concentration from 0 to 500 mM (Fig. 7a and b).<sup>71</sup> Second, profile fitting revealed the  $R^2$  coefficient = 0.996 and detection limit = 9.27  $\mu\text{M}$  at 0–170  $\mu\text{M}$  (inset, Fig. 7b), a value which is as accurate as that in reported data.<sup>72,73</sup> PL quenching is due to the interaction of  $\text{Fe}^{3+}$  with oxygenated and amino groups of CQDs (Fig. S2, ESI<sup>†</sup>), and therefore, instead of returning to ground states, excited photoelectrons are transferred to half-filled  $3d^5$  orbitals of cations.<sup>74</sup> The  $\text{Fe}^{3+}$  selectivity was further verified by treating HR15 with  $\text{Fe}^{3+}$ ,  $\text{Fe}^{2+}$ ,  $\text{Na}^+$ ,  $\text{K}^+$ ,  $\text{Mg}^{2+}$ ,  $\text{Ca}^{2+}$ ,  $\text{Co}^{2+}$ ,  $\text{Ni}^{2+}$ ,  $\text{Cu}^{2+}$ ,  $\text{Zn}^{2+}$ ,  $\text{Cr}^{3+}$ , and  $\text{Pb}^{2+}$  using the same concentrations and conditions (Fig. 7c). Clearly, a significant  $E_1$  decrease occurred only in  $\text{Fe}^{3+}$  aqueous solution, while others displayed a limited quenching effect. The small  $E_1$  decrease in  $\text{Co}^{2+}$ ,  $\text{Ni}^{2+}$ ,  $\text{Cu}^{2+}$ , and  $\text{Cr}^{3+}$  may originate from the binding between carboxylic groups and cations.<sup>75</sup>

### 3.4 CQD-made QR codes and trademarks

Quick response (QR) codes are optical labels widely used in admission control, process management, labelling, and packaging of merchandise. However, they can be copied and counterfeited without distortion through screenshots. Here, we demonstrate for the first time CQD-made QR codes, which are only recognized by UV irradiation. Fig. 8a and b demonstrates a low distortion transfer of CQD (HR15) ink from a QR-coded stamp to an ordinary piece of paper (<http://www.lib.nthu.edu.tw/>) (Fig. 8c). Because CQDs are hydrophilic

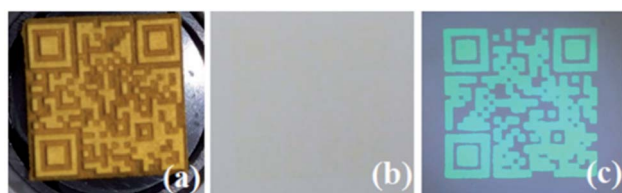


Fig. 8 (a) QR-coded stamp and HR15-QR-coded paper under (b) dark and (c) bright conditions.

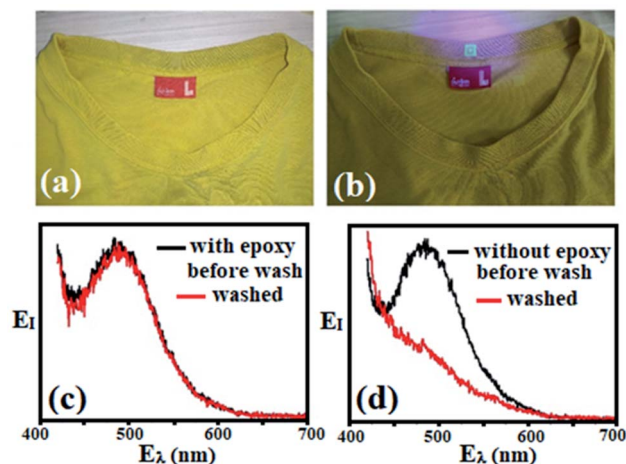


Fig. 9 A washed cotton fabric with an epoxy-HR15 coating under (a) dark and (b) bright conditions. Comparison of  $E_1$ - $E_\lambda$  plots of CQDs (c) with and (d) without epoxy coating before (dark) and after repeated washes (red).

and fade away with repeated washings (*i.e.*, fastness to washing (FTW)), experiments were then carried out to promote FTW as follows. First, CQDs were dispersed in epoxy-ethanol solution with a ratio of epoxy/curing agent/ethanol = 3 : 1.5 : 100. It is worth mentioning that epoxy is a thermoset polymer with wear durability and is therefore used as a protective coating. Second, CQDs/epoxy ethanol ink was thermally coated onto synthetic fabrics. Fig. 9a displays a repeatedly washed cotton fabric with an epoxy ink coating in the dark. Upon 395 nm illumination, the PL trademark appears, which is indicative of improved FTW (Fig. 9b). Comparison was also made for CQDs with and without epoxy coatings. Clearly, epoxy-coated CQDs display a similar  $E_1$  at  $E_{\lambda\text{C}} = 500$  nm before and after repeated washings (Fig. 9c). CQDs without epoxy protection, in contrast, completely disappear after washings and do not emit any PL (Fig. 9d).

## 4 Conclusions

HR-made CQDs emit green-blue light with high QY, thermal stability at  $\leq 150$  °C, and controllable  $E_1$  and  $E_\lambda$  through UA/CA adjustment. UA serves as a nitrogen source, and the N-doping content  $\propto$  UA/CA was verified. Applications of CQDs were demonstrated, including PL polymer/fibres, stealth QR coding, and labelling at the visible regime, as well as excellent sensing of  $\text{Fe}^{3+}$  in aqueous solution.

## Author contributions

All authors contributed equally to the manuscript.

## Conflicts of interest

The authors declare no competing financial interests.



## Acknowledgements

The authors thank the Ministry of Science and Technology of Taiwan for the financial support (MOST-109-2811-M-007-570). This work is also supported by the "High Entropy Materials Centre" from the Featured Areas Research Centre Program within the framework of the Higher Education Sprout Project by the Ministry of Education (MOE) in Taiwan (108QR001J4). The authors also acknowledge the use of F200 HRTEM and ARM200 Cs TEM, which belong to Instrumentation Centre at NTHU under funding by the Ministry of Science and Technology, Taiwan.

## Notes and references

- W. Li, Y. Yang, J. Fu, Z. Lin and J. He, *ES Energy Environ.*, 2019, **7**, 40–47, Special Topic on Thermal Metamaterials II, .
- V. P. Bhalekar, P. K. Baviskar, M. B. Rajendra Prasad, B. M. Palve, V. S. Kadam and H. M. Pathan, *Eng. Sci.*, 2019, **7**, 38–42.
- W. Wang, J. Li, P. Ni, B. Liu, Q. Chen, Y. Lu, H. Wu, B. Cao and Z. Liu, *ES Mater. Manuf.*, 2019, **4**, 66–73.
- D. Han, H. Mei, S. Xiao and L. Cheng, *Adv. Compos. Hybrid Mater.*, 2019, **2**, 142–150.
- T. K. Das, P. Ghosh and N. C. Das, *Adv. Compos. Hybrid Mater.*, 2019, **2**, 214–233.
- M. N. Uddin, H. T. N. Gandy, M. M. Rahman and R. Asmatulu, *Adv. Compos. Hybrid Mater.*, 2019, **2**, 339–350.
- M. Ramezankhani, B. Crawford, H. Khayyam, M. Naebe, R. Seethaler and A. S. Milani, *Adv. Compos. Hybrid Mater.*, 2019, **2**, 444–455.
- L. Zhao, Q. Ge, J. Sun, J. Peng, X. Yin, L. Huang, J. Wang, H. Wang and L. Wang, *Adv. Compos. Hybrid Mater.*, 2019, **2**, 481–491.
- F. Saba, S. A. Sajjadi, S. Heydari, M. Haddad-Sabzevar, J. Salehi and H. Babayi, *Adv. Compos. Hybrid Mater.*, 2019, **2**, 540–548.
- Y. Lu, G. Yu, X. Wei, C. Zhan, J.-W. Jeon, X. Wang, C. Jeffries, Z. Guo, S. Wei and E. K. Wujcik, *Adv. Compos. Hybrid Mater.*, 2019, **2**, 711–719.
- M. J. Islam, M. J. Rahman and T. Mieno, *Adv. Compos. Hybrid Mater.*, 2020, **3**, 285–293.
- S. O. Mirabootalebi, *Adv. Compos. Hybrid Mater.*, 2020, **3**, 336–343.
- Q. Xu, T. Kuang, Y. Liu, L. Cai, X. Peng, T. Sreenivasan Sreepasad, P. Zhao, Z. Yu and N. Li, *J. Mater. Chem. B*, 2016, **4**, 7204–7219.
- L. Ai, Y. Yang, B. Wang, J. Chang, Z. Tang, B. Yang and S. Lu, *Sci. Bull.*, 2021, **66**, 839–856.
- X. Ma, W. Zhong, J. Zhao, S. L. Suib and Y. Lei, *Eng. Sci.*, 2019, **9**, 44–49.
- A. Chandra and N. Singh, *Chem. Commun.*, 2018, **54**, 1643–1646.
- S. Lu, L. Sui, J. Liu, S. Zhu, A. Chen, M. Jin and B. Yang, *Adv. Mater.*, 2017, **29**, 1603443.
- S. Kalytchuk, Y. Wang, K. Poláková and R. Zbořil, *ACS Appl. Mater. Interfaces*, 2018, **10**, 29902–29908.
- H. Li, R. Liu, S. Lian, Y. Liu, H. Huang and Z. Kang, *Nanoscale*, 2013, **5**, 3289–3297.
- X. Huang, L. Yang, S. Hao, B. Zheng, L. Yan, F. Qu, A. M. Asiri and X. Sun, *Inorg. Chem. Front.*, 2017, **4**, 537–540.
- N. Wang, Z. X. Liu, R. S. Li, H. Z. Zhang, C. Z. Huang and J. Wang, *J. Mater. Chem. B*, 2017, **5**, 6394–6399.
- S. Liu, J. Tian, L. Wang, Y. Zhang, X. Qin, Y. Luo, A. M. Asiri, A. O. Al-Youbi and X. Sun, *Adv. Mater.*, 2012, **24**, 2037–2041.
- W. Lu, X. Qin, S. Liu, G. Chang, Y. Zhang, Y. Luo, A. M. Asiri, A. O. Al-Youbi and X. Sun, *Anal. Chem.*, 2012, **84**, 5351–5357.
- S. Li, D. Amat, Z. Peng, S. Vanni, S. Raskin, G. De Angulo, A. M. Othman, R. M. Graham and R. M. Leblanc, *Nanoscale*, 2016, **8**, 16662–16669.
- W. Zhou, J. Zhuang, W. Li, C. Hu, B. Lei and Y. Liu, *J. Mater. Chem. C*, 2017, **5**, 8014–8021.
- Y. Ma, H. Zhang, Y. Zhang, R. Hu, M. Jiang, R. Zhang, H. Lv, J. Tian, L. Chu, J. Zhang, Q. Xue, H.-L. Yip, R. Xia, X. a. Li and W. Huang, *ACS Appl. Mater. Interfaces*, 2019, **11**, 3044–3052.
- Q.-Y. Li, *ES Mater. Manuf.*, 2021, **12**, 1–2.
- A. Bhorde, R. Waykar, S. R. Rondiya, S. Nair, G. Lonkar, A. Funde, N. Y. Dzade and S. S. Jadhkar, *ES Mater. Manuf.*, 2021, **12**, 43–52.
- H. liang, X. Zhang, B. Lin, F. Wang, Z. Cheng, X. Shi and B. G. Lougou, *ES Energy Environ.*, 2020, **10**, 22–33.
- D. Wang and Z. Guo, *Eng. Sci.*, 2020, **11**, 1–2.
- X. Xu, R. Ray, Y. Gu, H. J. Ploehn, L. Gearheart, K. Raker and W. A. Scrivens, *J. Appl. Chem. Sci.*, 2004, **126**, 12736–12737.
- Y.-P. Sun, B. Zhou, Y. Lin, W. Wang, K. A. S. Fernando, P. Pathak, M. J. Mezziani, B. A. Harruff, X. Wang, H. Wang, P. G. Luo, H. Yang, M. E. Kose, B. Chen, L. M. Veca and S.-Y. Xie, *J. Appl. Chem. Sci.*, 2006, **128**, 7756–7757.
- L. Wang, X. Chen, Y. Lu, C. Liu and W. Yang, *Carbon*, 2015, **94**, 472–478.
- P. Wu, W. Li, Q. Wu, Y. Liu and S. Liu, *RSC Adv.*, 2017, **7**, 44144–44153.
- W. Li, Y. Liu, B. Wang, H. Song, Z. Liu, S. Lu and B. Yang, *Chin. Chem. Lett.*, 2019, **30**, 2323–2327.
- B. Wang, J. Li, Z. Tang, B. Yang and S. Lu, *Sci. Bull.*, 2019, **64**, 1285–1292.
- A. Chae, Y. Choi, S. Jo, Nur'aeni, P. Paoprasert, S. Y. Park and I. In, *RSC Adv.*, 2017, **7**, 12663–12669.
- J. Hou, W. Wang, T. Zhou, B. Wang, H. Li and L. Ding, *Nanoscale*, 2016, **8**, 11185–11193.
- H. Liu, T. Ye and C. Mao, *Angew. Chem., Int. Ed.*, 2007, **46**, 6473–6475.
- C. Hou, B. Wang, V. Murugadoss, S. Vupputuri, Y. Chao, Z. Guo, C. Wang and W. Du, *Eng. Sci.*, 2020, **11**, 19–30.
- S. H. Khan, B. Pathak and M. H. Fulekar, *Adv. Compos. Hybrid Mater.*, 2020, **3**, 551–569.
- Y. Liu, L. Jiang, B. Li, X. Fan, W. Wang, P. Liu, S. Xu and X. Luo, *J. Mater. Chem. B*, 2019, **7**, 3053–3058.
- W.-S. Kuo, C.-Y. Chang, K.-S. Huang, J.-C. Liu, Y.-T. Shao, C.-H. Yang and P.-C. Wu, *Int. J. Mol. Sci.*, 2020, **21**.
- W. Liu, R. Zhang, Y. Kang, X.-y. Zhang, H.-j. Wang, L.-h. Li, H.-p. Diao and W.-l. Wei, *New Carbon Mater.*, 2019, **34**, 390–402.



- 45 S. Liao, X. Li, H. Yang and X. Chen, *Talanta*, 2019, **194**, 554–562.
- 46 H. Shah, Q. Xin, X. Jia and J. R. Gong, *Arabian J. Chem.*, 2019, **12**, 1083–1091.
- 47 J. Zhang, X. Chen, Y. Li, S. Han, Y. Du and H. Liu, *Anal. Methods*, 2018, **10**, 541–547.
- 48 M. Zhou, Z. Zhou, A. Gong, Y. Zhang and Q. Li, *Talanta*, 2015, **143**, 107–113.
- 49 L. Fang, L. Zhang, Z. Chen, C. Zhu, J. Liu and J. Zheng, *Mater. Lett.*, 2017, **191**, 1–4.
- 50 T. Yoshinaga, Y. Iso and T. Isobe, *J. Lumin.*, 2019, **213**, 6–14.
- 51 P. Das, S. Ganguly, S. Mondal, M. Bose, A. K. Das, S. Banerjee and N. C. Das, *Sens. Actuators, B*, 2018, **266**, 583–593.
- 52 J. Schneider, C. J. Reckmeier, Y. Xiong, M. von Seckendorff, A. S. Susha, P. Kasák and A. L. Rogach, *J. Phys. Chem. C*, 2017, **121**, 2014–2022.
- 53 J. Zhu, X. Bai, J. Bai, G. Pan, Y. Zhu, Y. Zhai, H. Shao, X. Chen, B. Dong, H. Zhang and H. Song, *Nanotechnology*, 2018, **29**, 085705.
- 54 H. Ding, J.-S. Wei, N. Zhong, Q.-Y. Gao and H.-M. Xiong, *Langmuir*, 2017, **33**, 12635–12642.
- 55 Y. Liu, D. Chao, L. Zhou, Y. Li, R. Deng and H. Zhang, *Carbon*, 2018, **135**, 253–259.
- 56 A. N. Fletcher, *Photochem. Photobiol.*, 1969, **9**, 439–444.
- 57 Y. Fang, L. Zhou, J. Zhao, Y. Zhang, M. Yang and C. Yi, *Carbon*, 2020, **166**, 265–272.
- 58 H. Yang, Y. Liu, Z. Guo, B. Lei, J. Zhuang, X. Zhang, Z. Liu and C. Hu, *Nat. Commun.*, 2019, **10**, 1789.
- 59 A. B. Bourlinos, A. Stassinopoulos, D. Anglos, R. Zboril, M. Karakassides and E. P. Giannelis, *Small*, 2008, **4**, 455–458.
- 60 M. Zhang, H. Ju, L. Zhang, M. Sun, Z. Zhou, Z. Dai, L. Zhang, A. Gong, C. Wu and F. Du, *Int. J. Nanomed.*, 2015, **10**, 6943–6953.
- 61 K.-i. Sasaki, Y. Tokura and T. Sogawa, *Crystals*, 2013, **3**, 120–140.
- 62 Z. Feng, Z. Li, X. Zhang, Y. Shi and N. Zhou, *Molecules*, 2017, **22**, 2061.
- 63 L. Zhao, F. Di, D. Wang, L.-H. Guo, Y. Yang, B. Wan and H. Zhang, *Nanoscale*, 2013, **5**, 2655–2658.
- 64 A. N. Emam, S. A. Loutfy, A. A. Mostafa, H. Awad and M. B. Mohamed, *RSC Adv.*, 2017, **7**, 23502–23514.
- 65 Y. Wang, Q. Su and X. Yang, *Chem. Commun.*, 2018, **54**, 11312–11315.
- 66 P. Gombert, H. Biauget, R. de Seze, P. Pandard and J. Carré, *Int. J. Speleol.*, 2017, **46**, 23–31.
- 67 R. Hardman, *Environ. Health Perspect.*, 2006, **114**, 165–172.
- 68 Y. Wang, Y. Zhu, J. Huang, J. Cai, J. Zhu, X. Yang, J. Shen, H. Jiang and C. Li, *J. Phys. Chem. Lett.*, 2016, **7**, 4253–4258.
- 69 X. Wu, W. Li, P. Wu, C. Ma, Y. Liu, M. Xu and S. Liu, *Eng. Sci.*, 2018, **4**, 111–118.
- 70 Y. Chen, Y. Wu, B. Weng, B. Wang and C. Li, *Sens. Actuators, B*, 2016, **223**, 689–696.
- 71 W. Liu, H. Diao, H. Chang, H. Wang, T. Li and W. Wei, *Sens. Actuators, B*, 2017, **241**, 190–198.
- 72 H. Ding, J.-S. Wei and H.-M. Xiong, *Nanoscale*, 2014, **6**, 13817–13823.
- 73 H. A. Molla, R. Bhowmick, A. Katarkar, K. Chaudhuri, S. Gangopadhyay and M. Ali, *Anal. Methods*, 2015, **7**, 5149–5156.
- 74 Y. Li, Y. Liu, X. Shang, D. Chao, L. Zhou and H. Zhang, *Chem. Phys. Lett.*, 2018, **705**, 1–6.
- 75 F. Yan, Y. Zou, M. Wang, X. Mu, N. Yang and L. Chen, *Sens. Actuators, B*, 2014, **192**, 488–495.

